ACS Sustainable Chemistry & Engineering

Research Article

Cite This: ACS Sustainable Chem. Eng. 2018, 6, 12375−12384

pubs.acs.org/journal/ascecg

Tunable MoS_2/SnO_2 P−N Heterojunctions for an Efficient Trimethylamine Gas Sensor and 4-Nitrophenol Reduction Catalyst

Xiu-Qing Qiao,[†] Zhen-Wei Zhang,[†] Dong-Fang Hou,[†] Dong-Sheng Li,[*,†,‡] Yunlin Liu,[†] Ya-Qian Lan,[†] Jian Zhang,[‡] Pingyun Feng,[§] and Xianhui Bu[*,∥]

[†]College of Materials and Chemical Engineering, Hubei Provincial Collaborative Innovation Center for New Energy Microgrid, Key Laboratory of Inorganic Nonmetallic Crystalline and Energy Conversion Materials, China Three Gorges University, 8 University Road, Yichang 443002, Hube, PR China

[‡]State Key Laboratory of Structural Chemistry, Fujian Institute of Research on the Structure of Matter, Chinese Academy of Sciences, 155 yangqiao west road, Fuzhou 350002, Fujian, China

[§]Department of Chemistry, University of California, Riverside, California 92521, United States

[∥]Department of Chemistry and Biochemistry, California State University Long Beach, 1250 Bellflower Boulevard, Long Beach, California 90840, United States

Supporting Information

ABSTRACT: Synthetic design and construction of P−N heterojunctions are attracting increasing attention due to their potential applications such as in catalysis, gas sensors, and energy storage and conversion. In general, the design strategies of P−N heterojunctions target one specific property. The construction of multifunctional materials with different functions remains an interesting and challenging research pursuit. Especially, multifunctional properties switched within a given chemical combination have rarely been found. Herein, by adjusting the mole ratio between MoS_2 and SnO_2, the first bifunctional MoS_2/SnO_2 P−N heterojunctions have been realized within a particular chemical system. As a result of the combination of MoS_2 nanosheets and SnO_2 nanofibers, MoS_2/SnO_2 heterojunctions exhibit great potential in both gas sensors and catalysts. With low loading of MoS_2 (molar ratio, Mo/Sn = 0.53), the P−N heterojunction exhibits superior sensing selectivity and long-term stability toward trimethylamine. With increased MoS_2 amount, the P−N heterojunctions display very good catalytic activities for 4-nitrophenol reduction. The bifunctional MoS_2/SnO_2 P−N heterojunctions with high sensitivity, selectivity, stability, and catalytic activity are promising candidates for practical applications. It can be anticipated that the synthetic strategy reported here will create new opportunities for realizing multifunctional materials by the rational design of P−N heterojunctions.

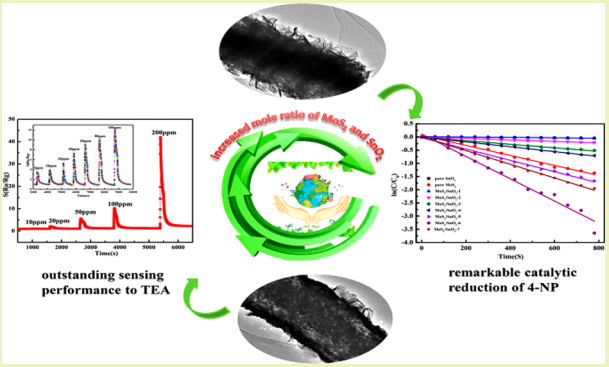

KEYWORDS: *MoS_2/SnO_2, P−N heterojunctions, Nanofiber, Nanosheet, Bifunctional, Triethanolamine sensor, Catalyst, 4-Nitrophenol*

INTRODUCTION

Heterojunctions have received renewed interest because they exhibit fascinating properties due to the synergetic effects between distinct components. Among various heterojunctions, P−N heterojunctions are the most studied ones because their efficient charge separation permit enhanced performance.[1−3] However, most of the P−N heterojunctions are constructed by tuning one component or morphology to target one particular function such as photocatalytic activity,[4,5] gas sensing,[6,7] or cell performance.[8] The construction of multifunctional materials with completely different functions by tuning the compositions within particular chemical system has been rarely found and remains an interesting and challenging research area.

For the rational design and synthesis of P−N heterojunctions, the components are always selected according to their intrinsic properties to enhance some specific properties. In particular, n-type SnO_2 has undoubtedly proven to be one of the most promising sensing material to toxic gases including H_2S, CO_2, CO, NO_2, NO, and some harmful vapors.[6] For example, various P−N heterojunctions including Co_3O_4−SnO_2,[9] NiO/SnO_2,[10] and CuO−SnO_2[11] with enhanced gas sensing behaviors have been successfully fabricated. However, to our best knowledge, multifunctional SnO_2 nanomaterials within one system have not been reported.

Molybdenum disulfide (MoS_2), an important 2D transition-metal dichalcogenide, has become a fascinating candidate to

Received: June 18, 2018
Revised: July 11, 2018
Published: July 25, 2018

DOI: 10.1021/acssuschemeng.8b02842
ACS Sustainable Chem. Eng. 2018, 6, 12375−12384

enhance catalytic and electrochemical performance.[12−16] Nowadays, lots of works have focused on the fabrication of MoS_2 based heterojunctions, utilizing the fancy properties of MoS_2. For example, Xing et al. prepared the N-TiO_{2-x}@MoS_2 heterojunctions via the combined hydrothermal−chemical reduction method, and the heterojunctions exhibited high visible-light catalytic activity.[17] Yang et al. reported novel P−N heterojunction $BiVO_4$@MoS_2 photocatalysts and showed high activities for catalytic Cr(VI) reduction and Crystal Violet oxidation.[18] These studies show the great potential of MoS_2 nanomaterials in designing P−N heterojunctions. Inspired by the works on MoS_2/SnO_2 gas sensors by Liu et al.[19] and Zhang et al.,[20] we hope to realize the construction of bifunctional P−N heterojunctions by combining SnO_2 (N-type) and MoS_2 (P-type) with distinct gas sensing and catalytic properties, respectively. Furthermore, vertically aligned MoS_2 nanosheets (NSs) with more active sites will be helpful for the further improvement of properties.[21]

Herein, we first fabricated one-dimensional (1D) porous SnO_2 nanofibers (NFs) via an electrospinning method and then vertically aligned MoS_2 NSs on the porous structure (denoted as MoS_2/SnO_2) to construct P−N heterojunctions. With our approach, bifunctional P−N heterojunctions with excellent gas sensing and catalytic properties were realized by simply varying the MoS_2 amount. When the loading of MoS_2 is low, MoS_2/SnO_2 heterojunction sensors exhibit high sensitivity, superior sensing selectivity, lower optimal working temperature, and long-term stability toward triethanolamine (TEA) vapor. With increasing MoS_2 amount, the P−N heterojunctions show outstanding performance for reducing 4-nitrophenol (4-NP). Mechanisms for the gas sensing and catalytic performance of the MoS_2/SnO_2 heterojunction were discussed in detail. The excellent properties of MoS_2/SnO_2 heterojunctions likely originate from the synergistic effect of hierarchical architectures, intimate contact of SnO_2 and Mos_2 in P−N heterojunctions, and abundant active sites.

■ EXPERIMENTAL SECTION

Chemicals. Stannous chloride ($SnCl_2·2H_2O$), absolute ethyl alcohol (C_2H_6O), *N*,*N*-dimethylformamide (DMF, C_3H_7NO), ammonium molybdate ($(NH_4)_6Mo_7O_{24}·4H_2O$), thiourea ($(NH_2)_2S$), 4-nitropheonol($C_6H_5NO_3$), and sodium borohydride ($NaBH_4$) were purchased from Sinopharm Chemical Reagent Co., Ltd. Poly(vinylpyrrolidone) (PVP, Mw = 1 300 000) was purchased from Sigma-Aldrich. No further purifications were performed.

Synthesis of Porous SnO_2 NFs. One-dimensional porous SnO_2 NFs were synthesized by an electrospinning process. Briefly, $SnCl_2·2H_2O$ (2.4 g) was dissolved into 20 mL mixed solution of ethanol and DMF (1:1 volume ratio) and stirred for 5 min, followed by addition of PVP (2.4 g) and stirring for another 12 h to form a homogeneous precursor solution. Subsequently, the obtained transparent solution was injected using a syringe with stainless steel needle (No. 20) and the feeding rate is 1 mL/h. The distance between the tip of the spinneret and the collector is 18 cm, and a constant voltage of 18 kV was kept. The collected as-spun fibers were dried in a muffle furnace and then sintered under different temperatures (300−600 °C) in air for 2 h at 1 °C min^{-1}.

Preparation of MoS_2/SnO_2 Hierarchical Heterojunctions. The MoS_2/SnO_2 heterojunctions were synthesized by hydrothermal method. SnO_2 NFs calcined at 600 °C (200 mg) were dispersed in DI water (40 mL) by sonication and then $(NH_4)_6Mo_7O_{24}·4H_2O$ (0.01 mmol) and CN_2H_4S (0.3 mmol) were added into the mixture. After stirring for 20 min, the solution was transferred to a 50 mL Teflon autoclave and heated at 210 °C for 12 h. The final powders were harvested after centrifugation, washing, and drying at 80 °C for 6 h. The heterojunction was named as MoS_2/SnO_2-1. MoS_2/SnO_2 heterojunctions with different mole ratios of Mo to Sn (R, Mo/Sn = 0.05, 0.26, 0.53, 0.79, 1.06, 1.32, 1.57) were successfully prepared following the similar way except for the amounts of S and Mo and denoted as MoS_2/SnO_2-1, MoS_2/SnO_2-2, MoS_2/SnO_2-3, MoS_2/SnO_2-4, MoS_2/SnO_2-5, MoS_2/SnO_2-6, and MoS_2/SnO_2-7, respectively. Moreover, pure MoS_2 NSs were prepared under identical conditions without the presence of porous SnO_2 NFs.

Microstructural Characterization. Thermogravimetric (TG) analysis was measured on a NETZSCH449C thermal analyzer (heating rate of 10 °C min^{-1}) under air. The crystal structure was studied by X-ray diffraction (XRD) patterns using Cu Kα radiation from 10° to 80°. The morphology and structure were observed on a JSM-7500F field emission scanning electron microscopy (FESEM). The energy dispersive spectroscopy (EDS) was introduced to identify the chemical composition. Transmission electron microscopy (TEM) measurements were conducted on the Tecnai G2 F20 S-TWIN with an acceleration voltage of 20 kV. Moreover, X-ray photoelectron spectroscopy (XPS) measurement was performed on an ESCALAB 250 X-ray instrument using monochromatic Al Kα source. The Brunauer−Emmett−Teller (BET) specific surface areas and pore size distributions of all the samples were analyzed from the nitrogen adsorption isotherms and Barret−Joyner−Halender (BJH) methods, respectively. UV−vis spectra was obtained from Shimadzu UV−vis 2550 spectrophotometer (Japan).

Fabrication and Test of Gas Sensors. A certain amount of powders were dispersed in ethanol with the weight ratio of 9:1 to form homogeneous paste. The paste was then brushed on the sensor substrates, on which Ag−Pd electrodes with 1 mm spacing were deposited. The coated paste was stabilized at 80 °C overnight. Gas sensing properties of the sensors to formaldehyde, methyl alcohol, ethyl alcohol, and triethanolamine (TEA) were tested on the intelligent gas sensing analysis system (CGS-4TP, Beijing Elite Tech Co. Ltd. China). The response was denoted by S = Ra/Rg, in which Ra is the resistance in atmospheric air, and Rg is the resistance in the tested gas. The testing temperature was from 180 to 290 °C. The concentrations of TEA were controlled at 5, 10, 20, 40, 60, 80, and 100 ppm, respectively.

Evaluation of the Catalytic Reduction for 4-NP. The catalytic reduction properties were estimated by chemical reduction of 4-NP to 4-AP with $NaBH_4$. In a typical experiment, $NaBH_4$ (1.6 mg) was added into 4-NP aqueous solution (0.1 mM, 3 mL) and a color change from light yellow to yellow-green was observed resulting from the generation of *p*-nitrophenolate under alkaline condition. Then, MoS_2/SnO_2 P−N heterojunction (1.5 mg) was introduced into the above solution and the peak change within 200−500 nm was immediately recorded on the UV−vis spectrophotometer. The catalytic reduction of 4-NP to 4-AP can be determined by the decrease of 400 nm peak with the appearance of 297 nm peak.

■ RESULTS AND DISCUSSION

Synthesis and Structural Analysis. MoS_2/SnO_2 hierarchical heterojunctions were prepared via the combined "electrospun−hydrothermal" processes (Figure 1). To optimize the synthesis parameters of SnO_2 NFs, TG, XRD, and SEM were performed (Figures S1−S3). The sample calcined at 600 °C was polycrystalline SnO_2 with hollow porous structure (Figure S2i, j), which is favorable for excellent properties.[22] The rutile structure of polycrystalline SnO_2 NFs was confirmed by XRD (Figure S3) and select area electron diffraction (SAED) pattern (Figure 2a, inset). The SEM and TEM images of the as-synthesized SnO_2 NFs are shown in Figures S2i, j and 2a, b. Highly porous SnO_2 hollow fibers consisted of small nanoparticles, which are capable of facilitating material transportation when used in related applications were obtained.[23] Because of the porous hollow structure and the heterogeneous nucleation, MoS_2 ultrathin NSs can be

DOI: 10.1021/acssuschemeng.8b02842
ACS Sustainable Chem. Eng. 2018, 6, 12375−12384

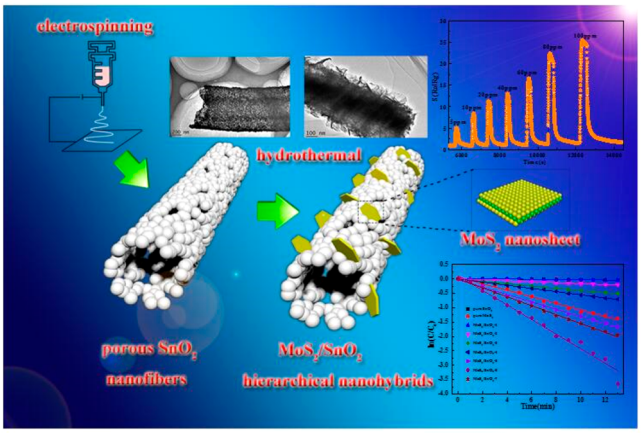

Figure 1. Illustration of the fabrication of MoS_2/SnO_2 heterojunctions and their properties.

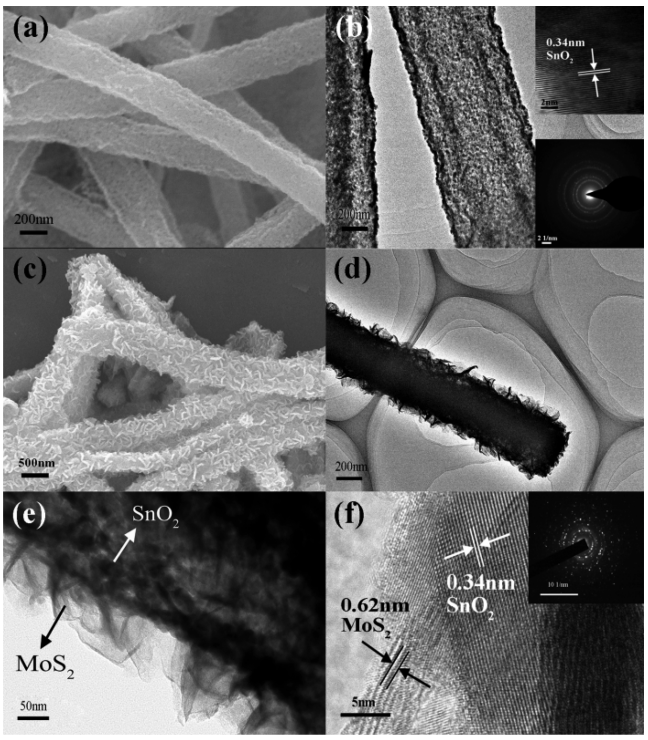

Figure 2. (a) SEM and (b) HRTEM image of SnO_2 NFs. (c) SEM, (d) TEM, and (e, f) HRTEM image of the MoS_2/SnO_2-3 heterojunction.

uniformly decorated on the SnO_2 NFs, leading to effective functionalization of SnO_2.

We demonstrate here that by controlling the amount of $(NH_4)_6Mo_7O_{24}\cdot 4H_2O$ and CN_2H_4S, and hence the ratio of Mo to Sn (R, Mo/Sn) from 0.05 to 1.57, it is possible to obtain dual functional MoS_2/SnO_2 hierarchical heterojunctions. Under hydrothermal conditions, MoS_2 NSs will heterogeneously nucleate and grow on the porous sites of SnO_2 nanofibers (NFs), and hence vertically grown MoS_2 NSs on SnO_2 NFs can be obtained. As shown in Figure 2c−f, the MoS_2/SnO_2-3 heterojunction (R = 0.1) with MoS_2 NSs are uniformly attached onto the surface of SnO_2 NFs, creating an ultrathin structure with lots of edge exposure perpendicularly grown to the SnO_2 NFs. Moreover, MoS_2 NSs and SnO_2 with clear lattice fringes are calibrated in the HRTEM image (Figure 2f). Interplanar crystal spacing of 0.34 nm corresponds to the (110) plane of SnO_2 while lattice spacing of 0.62 nm can be indexed as the (002) crystallographic plane of MoS_2 NSs, respectively.[24] With lower R values, inferior MoS_2 NSs coverage can be observed (Figure S4a), while dense coverages of MoS_2 NSs on the SnO_2 NFs were formed with $R \geq 0.53$ (Figure S4e−g). Importantly, no unsupported MoS_2 NSs can be detected in all the samples and only dispersive MoS_2 NSs were obtained without SnO_2 nanofibers (Figure S4h) further demonstrating the preferential heterogeneous nucleation of MoS_2 on the porous SnO_2 NFs.[25] Moreover, the EDS element mapping analysis (Figure S5) provides more evidence for the uniform distribution of MoS_2 NSs on SnO_2 NFs.

All the specimens were identified by XRD patterns as having the tetragonal rutile SnO_2 structure (JCPDS card no. 41-1445) (Figure S6).[26] Meanwhile, very weak diffraction peaks belonging to MoS_2 can be observed with high R values, probably because of the ultrathin structure or weak crystallization of MoS_2 NSs.[25,27] In addition, XPS spectra survey of SnO_2, MoS_2, and MoS_2/SnO_2-3 heterojunction were deconvoluted to analyze the chemical structure changes. As expected, peaks of Sn, Mo, O, and S can be clearly observed (Figure S7) in the MoS_2/SnO_2-3 heterojunction, giving evidence for the loading of MoS_2 NSs onto SnO_2. The two peaks of Sn 3d region at 487.1 eV (Sn $3d_{5/2}$) and 495.5 eV (Sn $3d_{3/2}$), together with the peak of O 1s region at 531.1 eV are certified as typical characteristic peaks of SnO_2 (Figure 3a, b).[28] Additionally, the peak centered at 532.4 eV can be attributed to the oxygen species originating from the adsorbed oxygen or hydroxyl ions.[29] It has been suggested that the presence of oxygen species on the surface helps enhance the sensitivities of gas sensors,[30] thus allowing the MoS_2/SnO_2-3 heterojunction to possess significant advantages in gas sensor applications, which will be discussed later. From the high-resolution XPS spectrum of Mo 3d (Figure 3c), the binding energies found at 228.6 and 231.8 eV can be assigned to Mo^{4+} $3d_{5/2}$ and $3d_{3/2}$, suggesting that Mo^{4+} exists in the MoS_2/SnO_2 heterojunction.[31] This is further confirmed by the presence of the S $2p_{3/2}$ and S $2p_{1/2}$ orbitals of S^{2-} ions centered at 161.5 and 162.7 eV (Figure 3d). Meanwhile, the peaks near 233.0 and 236.0 eV are attributed to the oxidation state of the Mo atoms, possibly from the partial oxidation of MoS_2.[32,33] Interestingly, after MoS_2 NSs are decorated onto the SnO_2 NFs, the corresponding peaks of S 2p and Mo 3d shift negatively compared with pure MoS_2, while the peaks of Sn 3d and O 1s shift positively compared with blank SnO_2 (Figure 3e−h), indicating a strong interaction between SnO_2 and MoS_2. The XPS result further shows the intimate growth of ultrafine MoS_2 NSs on the SnO_2 surfaces.

The BET specific surface areas and BJH pore size distributions of SnO_2, MoS_2/SnO_2-3, and MoS_2/SnO_2-6 heterojunctions were measured from N_2 adsorption at 77 K (Figure S8). By growing MoS_2 NSs on the SnO_2 NFs, the surface areas and pore volumes of MoS_2/SnO_2 heterojunctions are significantly decreased than those of the bare SnO_2 NFs (Table S1). In addition, the mesoporous structure SnO_2 NFs with the maximum distribution around 15 nm originating from pores between the small SnO_2 nanoparticles. In contrast, the pore sizes of MoS_2/SnO_2 heterojunctions are mainly distributed from 1 to 10 nm. This is apparently because of the partial coverage of porous SnO_2 NFs from the heterogeneous nucleation and growth of MoS_2 onto the porous sites.

DOI: 10.1021/acssuschemeng.8b02842
ACS Sustainable Chem. Eng. 2018, 6, 12375−12384

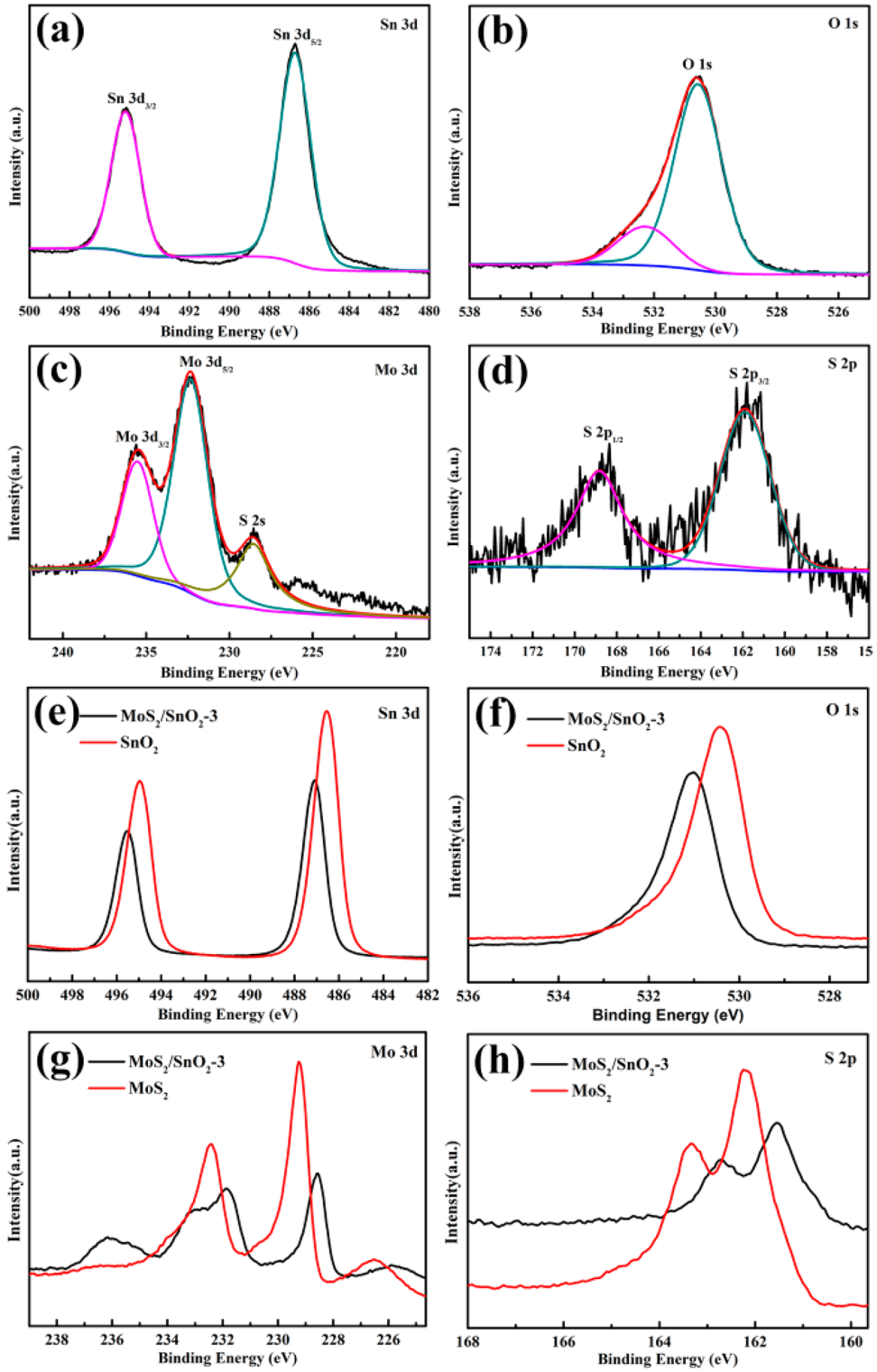

Figure 3. (a) Narrow scan XPS spectra of the elements (b) Sn, (c) O, (d) Mo, and (e) S of the MoS_2/SnO_2-3 heterojunction. (e) Sn 3d peaks, (f) O 1s peaks, (g) Mo 3d peaks, and (h) S 2p peaks of pure MoS_2 and the MoS_2/SnO_2-3 heterojunction.

Gas Sensing Properties and the Mechanism. The responses of all the sensors to TEA (200 ppm) as a function of the operating temperatures are shown in Figure S9. Clearly MoS_2/SnO_2 heterojunction sensors show a much more enhanced response than pure SnO_2 NFs from 180 to 290 °C. As the temperature goes up, the responses initially increase and subsequently decrease with the optimum working temperature (OWT) of MoS_2/SnO_2 gas sensors at 230 °C and SnO_2 NFs at 270 °C. Obviously, the OWT of MoS_2/SnO_2 gas sensors was effectively reduced. The gradual decreases in response after 230 °C for MoS_2/SnO_2 heterojunction sensors might result from the competing process related to desorption of the chemisorbed oxygen.[34] Specifically, the MoS_2/SnO_2-3 heterojunction sensor exhibits the maximum response values of

DOI: 10.1021/acssuschemeng.8b02842
ACS Sustainable Chem. Eng. 2018, 6, 12375−12384

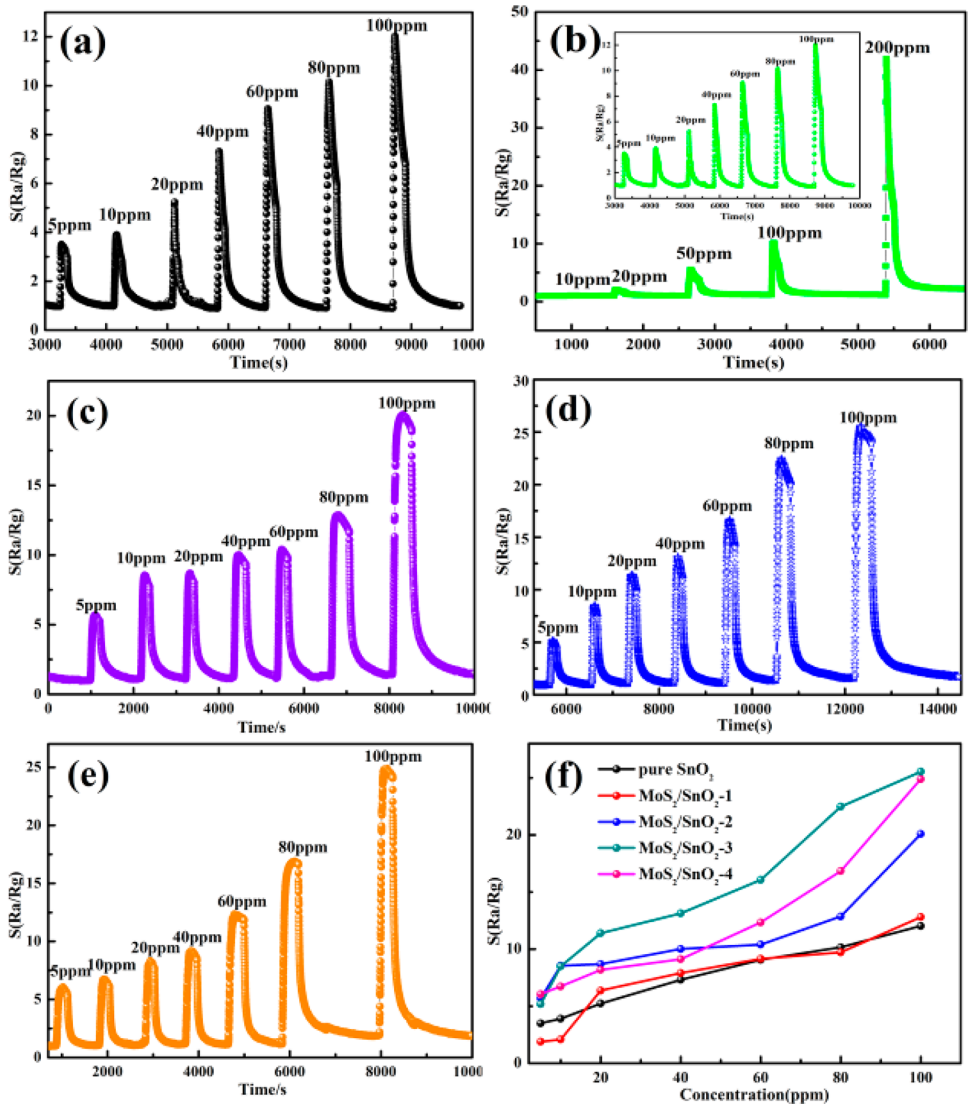

Figure 4. (a) Dynamic response of pure SnO_2 NFs sensor, (b) MoS_2/SnO_2-1 heterojunction, (c) MoS_2/SnO_2-2 heterojunction, (d) MoS_2/SnO_2-3 heterojunction, and (e) MoS_2/SnO_2-4 heterojunction toward various TEA concentrations at 230 °C. (f) Correlation between gas concentrations and sensitivity of all samples at 230 °C.

106.3 toward 200 ppm TEA at 230 °C, approximately 11 times the value of the SnO_2 sensor (9.7). However, further increasing the loading amounts of MoS_2 (MoS_2/SnO_2-5, MoS_2/SnO_2-6, MoS_2/SnO_2-7) resulted in the instability and decreased responses (not shown in the paper), which may be caused by the thermal instability of MoS_2 NSs.[35] Figure 4 gives the dynamic TEA sensing properties of all the sensors with concentrations varied from 5 to 100 ppm at 230 °C. The MoS_2/SnO_2-3 sensor exhibits the highest responses to various TEA concentrations, and the value toward 100 ppm of TEA gas is 24.9. In addition, all sensors are sensitive to TEA gas with detection limit of 5 ppm (S = 6.0) in our tests, and linear relationships between the response and TEA concentrations are observed (Figure S10). The fact that the response of MoS_2/SnO_2 heterojunction sensors toward TEA gases are greatly enhanced over that of pure SnO_2 NFs may be caused by more important contributions rather than surface area (Figure S8, Table S1), which is discussed in the following section.

The reproducibility of the MoS_2/SnO_2-3 heterojunction sensor to 100 ppm TEA was studied for seven cycles (Figure 5a). Evidently, the sensor exhibits consistent sensing responses even after seven cycles and the response magnitude is very close to that of the first run without clear attenuation, indicating that the MoS_2/SnO_2-3 sensor possesses good reversibility and repeatability. Moreover, the stability of the sensor over 2 months (Figure 5b) confirmed the superior long-term stability of the MoS_2/SnO_2 sensor devices.

Moreover, in order to determine the selectivity of MoS_2/SnO_2 heterojunction sensors, gas sensing experiments were performed toward various gas species, i.e., TEA ($C_6H_{15}O_3N$), formaldehyde (HCHO), acetone (C_3H_6O), ethanol (C_2H_5OH), and methanol (CH_3OH) at 200 ppm and 230 °C. The results in Figure 5d demonstrate the MoS_2/SnO_2-3 sensor exhibits markedly higher response toward TEA, whereas the SnO_2 sensor exhibits comparable response to the interfering vapors (Figure 5c). The result suggests the MoS_2 decoration on SnO_2 NFs can greatly enhance the selectivity toward TEA vs other gases. Although the exact reason remains unclear, it is possible that the three ethyl groups of TEA lead to the strongest electron-donating ability among the various tested gases. Also, the N atom in TEA uses its lone pair

DOI: 10.1021/acssuschemeng.8b02842
ACS Sustainable Chem. Eng. 2018, 6, 12375−12384

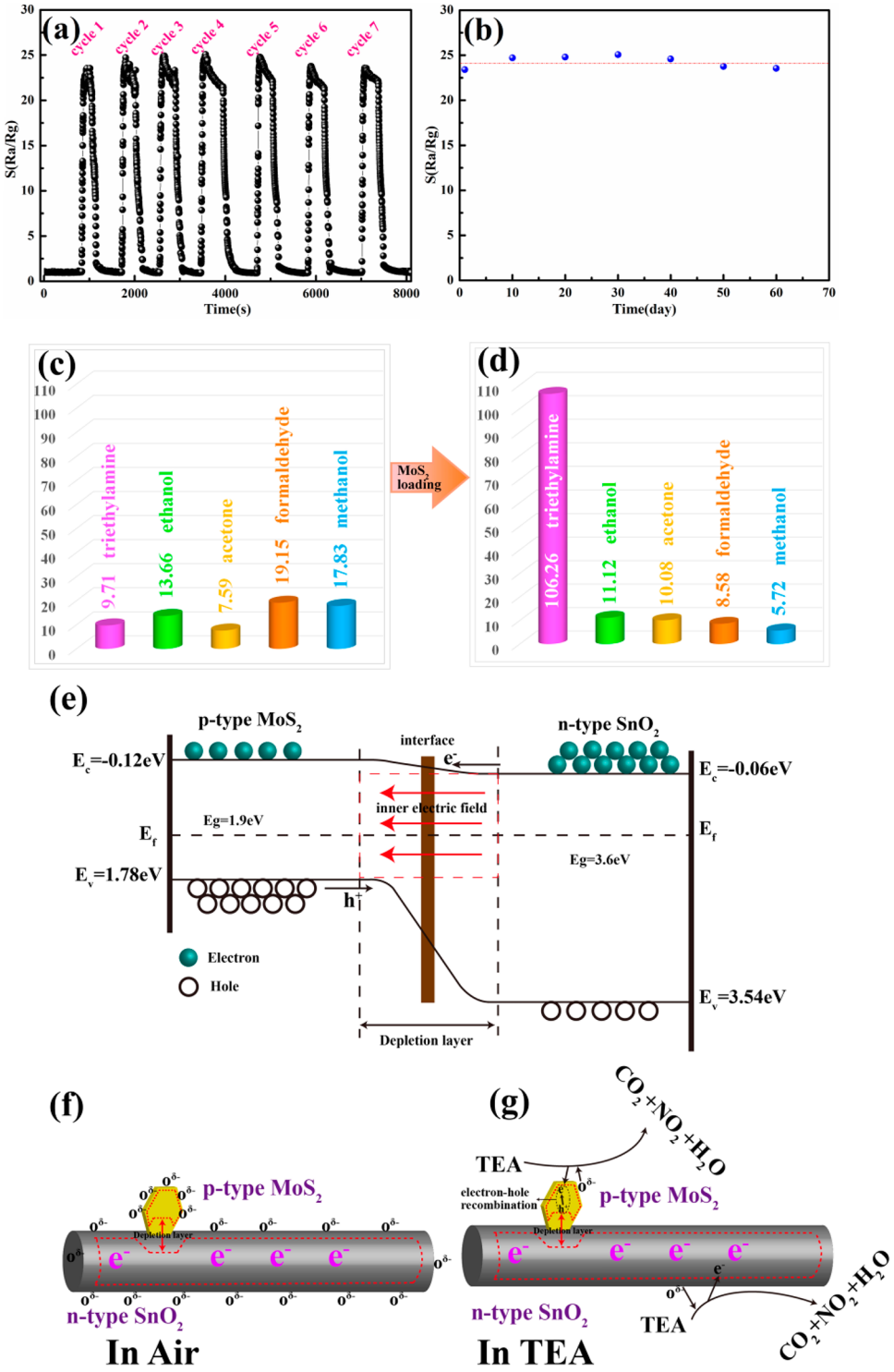

Figure 5. (a) Sensing reproducibility of the MoS_2/SnO_2-3 hierarchical heterojunction sensor to 100 ppm TEA concentrations. (b) Stability of the MoS_2/SnO_2 gas sensor. (c) Gas responses of pure SnO_2 sensor and (d) MoS_2/SnO_2-3 heterojunction sensor toward 200 ppm various gases. (e) Schematic illustration of energy band of MoS_2/SnO_2 heterojunctions. Model for the MoS_2/SnO_2 heterojunction sensors in air (f) and TEA vapor (g).

electrons to form bonds.[36] Thus, the TEA molecules are more likely to be adsorbed onto Lewis-acid (Mo ion) sites, particularly at 230 °C, resulting in the superior sensing selectivity of MoS_2/SnO_2 heterojunctions.

Collectively, the MoS_2/SnO_2 heterojunction sensors show high response, lower OWT, outstanding reproducibility, excellent long-term stability, and good selectivity toward TEA gases. To demonstrate the advantages of the MoS_2/SnO_2 heterojunction sensors, the sensing properties are compared with some reported sensors, as summarized in Table S2, which show the impressive performances as the materials reported here. Considering these results, this created MoS_2/SnO_2 heterojunctions show potential promising prospect for the selective detection of TEA vapor.

DOI: 10.1021/acssuschemeng.8b02842
ACS Sustainable Chem. Eng. 2018, 6, 12375−12384

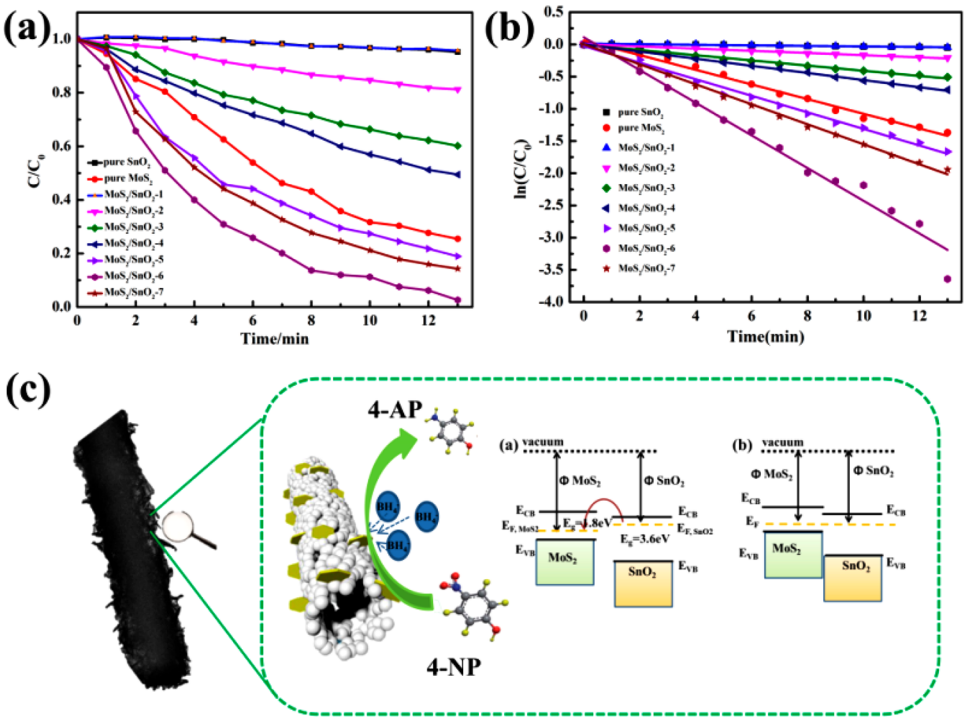

Figure 6. (a) Plots of C/C_0 and (b) $\ln(C/C_0)$ vs reaction time for the reduction of 4-NP over different catalysts. (c) Proposed mechanism for 4-NP reduction over MoS_2/SnO_2 heterojunctions.

Based on our experimental results, we suggest a tentative mechanism for the improvement of sensing performance of the MoS_2/SnO_2 based materials (Figure 5e–g). The gas sensing mechanism of N-type SnO_2 sensor can be well explained with the space–charge or depletion layer model.[37–39] For the MoS_2/SnO_2 heterojunction sensors, the mechanism is different. The elevated sensing properties may attribute to three factors. First, the responses S (S = Ra/Rg) to TEA are greatly enhanced owing to the formation of P–N heterojunction. As shown in Figure 5e, the work function (W) of MoS_2 is 5.2–5.39 eV,[40] which is higher than the value of SnO_2 (4.9 eV),[41,42] resulting in the electrons transfer from SnO_2 to MoS_2 until the Fermi level (E_f) is equalized. Benefiting from the tight P–N heterojunctions and the relative low potential barrier, the charge transfer will be much easier. Electrons migrate from SnO_2 to MoS_2 while holes flow from MoS_2 to SnO_2,[43] which will result in the formation of the space-charge region. Thus, the energy band will bend in the region and establish an internal electric field near the interface (Figure 5e). The increased electron concentrations on the sensor's surface will facilitate the oxygen adsorption, resulting higher barrier height and resistance. The higher resistance of the MoS_2/SnO_2 heterojunctions in air (Ra) derives from the formation of P–N heterojunction and depletion layer near the interface (Figure 5f). When contacted with TEA vapor, the TEA gas molecules will interact with the adsorbed oxygen species $O^{\delta-}$ (O^{2-}, O^-, O_2^-) by the following equation:[44]

$$(C_2H_5)_3N + O^{\delta-} \leftrightarrow NO_2 + H_2O + CO_2 + e^- \quad (1)$$

In this process, electrons are released back to the SnO_2 NFs, resulting in the resistance further decreased. Furthermore, TEA molecules will release electrons into MoS_2 and decrease the holes concentration. On the basis of the famous law of mass action (for semiconductor, $n_0 \times p_0 = n_i$),[2,45] the reduce of holes in MoS_2 will leads to the raise of electrons, which will result in the decrease of the concentration gradient in the P–N heterojunction. As a result, the depletion layer and the barrier height was reduced near the interface. Therefore, the resistance of the MoS_2/SnO_2 heterojunction sensors in TEA was further decreased compared with blank SnO_2, as illustrated in Figure 5g. Thus, the response (S) to TEA will be greatly enhanced thanks to the formation of P–N heterojunction. Second, the hierarchical structure of vertically grown MoS_2 NSs on the porous structure of SnO_2 NFs, is favorable for the attacking possibilities of the test gases.[34,41] Lastly, thanks to the vertical growth of MoS_2 NSs, the fully exposed Mo sites contribute to the adsorption for TEA gas molecules and result in the high sensitivity and selectivity toward TEA.

Catalytic Activities and the Mechanism. The catalytic activities of MoS_2/SnO_2 heterojunctions were evaluated by the hydrogenation reduction of 4-NP to 4-AP in the presence of $NaBH_4$. We confirmed that this reaction did not occur without catalysts. Figure S11 displays the time-dependent UV–vis absorption spectra over all the samples. The strong absorbance peak at 400 nm show negligible decrease with time for the SnO_2 NFs, indicating the SnO_2 NFs are almost inert for the reduction of 4-NP. After decorated by MoS_2, the catalytic performances of SnO_2 were greatly enhanced. Furthermore, the catalytic activities first increase remarkably with increasing MoS_2 amount and then decrease, among which MoS_2/SnO_2-6 (R = 1.32) heterojunction catalyst exhibits the highest catalytic reduction efficiency, as shown in Figure 6. Obviously, even though SnO_2 NFs show a negligible activity, the MoS_2/SnO_2 catalysts exhibit much enhanced catalytic performance for the hydrogenation reduction of 4-NP, which may be caused by the synergistic effects of the heterojunction catalysts. Considering that the initial concentration of $NaBH_4$ is much higher than 4-NP, the catalytic reduction process over MoS_2/SnO_2 heterojunctions follows the pseudo first-order kinetics:[46,47]

DOI: 10.1021/acssuschemeng.8b02842
ACS Sustainable Chem. Eng. 2018, 6, 12375–12384

$$\ln(C_t/C_0) = -\kappa_{app}t \quad (2)$$

where C_0 is the concentration of 4-NP at initial time, C_t is the concentration at reaction time t. κ_{app} is the apparent rate constant (S^{-1}).

The plots of $\ln(C_t/C_0)$ versus time shown in Figure 6b show good linear correlations for all catalysts confirming the first-order reaction. The calculated maximum rate constant (κ_{app}) is $\kappa_{app} = 4.2 \times 10^{-3}$ S^{-1} for MoS_2/SnO_2-6 heterojunction. The value is about 59 times and 4.5 times higher than that of SnO_2 NFs (7.1×10^{-5} S^{-1}) and MoS_2 NSs (9.2×10^{-4} S^{-1}), respectively (Figure 6b). Interestingly, the catalytic activity of MoS_2/SnO_2-6 heterojunction in our study is much higher than several reported metal-based and metal-free catalysts (Table S3), implying the potential application as efficient metal-free catalyst.

Based on the experimental results, a conceivable mechanism for the catalysis by MoS_2/SnO_2 heterojunction catalysts is proposed, as illustrated in Figure 6c. BH_4^- anions will first adsorb onto the defect-rich active sites of MoS_2 NSs, providing electrons and hydrogen protons for the hydrogenation reduction of 4-NP. Meanwhile, 4-NP pollutants are also adsorbed onto MoS_2 NSs, which could be reduced into 4-AP with the assistance of hydrogen protons and electrons. In our work, the intimate contact of MoS_2 NSs and SnO_2 promote MoS_2 NSs shift to more negative Fermi level to achieve an equilibrium state with SnO_2 NFs, giving rise to higher catalytic activity than that of single MoS_2 NSs. Moreover, electrons (e) that flowed from the CB of SnO_2 NFs to the MoS_2 NSs have strong reduction ability to catalytic reduce 4-NP. With the electrons in the MoS_2 NSs incessantly increased, the Fermi level of MoS_2 NSs negatively shifts and produces electrons with stronger reducibility, accordingly further enhancing the catalytic activities of MoS_2/SnO_2 catalysts. So we believe that the enhanced catalytic activities of the MoS_2/SnO_2 heterojunction catalysts are attributed to not only the catalytic activity of MoS_2 NSs but also the formed intimate junctions with matched energy bands between MoS_2 NSs and SnO_2 NFs.

In conclusion, we successfully constructed bifunctional MoS_2/SnO_2 P−N heterojunctions with fantabulous gas sensing and catalytic properties by tuning the MoS_2 amount. With the low MoS_2 loading, MoS_2/SnO_2 hierarchical P−N heterojunctions exhibit high sensitivity, lower optimal working temperature, excellent sensing selectivity, and outstanding long-term stability toward TEA vapor. When the MoS_2 amount is higher, the MoS_2/SnO_2 P−N heterojunctions show much enhanced catalytic reduction of 4-NP, making them potential candidates act a highly efficient catalyst to replace noble metals. The enhancement of gas sensing and catalytic performances of the MoS_2/SnO_2 P−N heterojunctions may be attributed to the synergic effect of hierarchical structures, more exposed active sites, as well as the P−N heterojunctions. This work puts forward an innovative strategy to construct superior bifunctional heterojunctions. In combination with other functional materials, the synthetic method reported here can be used for developing a range of multifunctional materials.

■ ASSOCIATED CONTENT

Supporting Information

The Supporting Information is available free of charge on the ACS Publications website at DOI: 10.1021/acssuschemeng.8b02842.

Additional details including the TG, XRD, SEM of SnO_2, SEM and EDS of SnO_2/MoS_2, SEM of MoS_2, XRD, XPS, and BET of SnO_2/MoS_2, gas response, and UV−vis spectra of 4-NP (PDF)

■ AUTHOR INFORMATION

Corresponding Authors

*E-mail: lidongsheng1@126.com (D.-S.L.).
*E-mail: xianhui.bu@csulb.edu (X.B.).

ORCID

Dong-Sheng Li: 0000-0003-1283-6334
Yunlin Liu: 0000-0001-5040-6816
Ya-Qian Lan: 0000-0002-2140-7980
Jian Zhang: 0000-0003-3373-9621
Pingyun Feng: 0000-0003-3684-577X
Xianhui Bu: 0000-0002-2994-4051

Notes

The authors declare no competing financial interest.

■ ACKNOWLEDGMENTS

The research was financially supported by the National Natural Science Foundation (Nos. 51502155, 21373122, 51572152, 21671119, and 21673127), the Research Project of HPDE (No. D20151203), and the State Key Laboratory of Structural Chemistry, FJIRSM (20170020).

■ REFERENCES

(1) Kim, H. R.; Haensch, A.; Kim, I. D.; Barsan, N.; Weimar, U.; Lee, J. H. The Role of NiO Doping in Reducing the Impact of Humidity on the Performance of SnO_2-Based Gas Sensors: Synthesis Strategies, and Phenomenological and Spectroscopic Studies. *Adv. Funct. Mater.* **2011**, *21* (23), 4456−4463.

(2) Wang, H.; Zhang, L.; Chen, Z.; Hu, J.; Li, S.; Wang, Z.; Liu, J.; Wang, X. Semiconductor heterojunction photocatalysts: design, construction, and photocatalytic performances. *Chem. Soc. Rev.* **2014**, *43* (15), 5234−5244.

(3) Kumar, P. S.; Sundaramurthy, J.; Sundarrajan, S.; Babu, V. J.; Singh, G.; Allakhverdiev, S. I.; Ramakrishna, S. Hierarchical electrospun nanofibers for energy harvesting, production and environmental remediation. *Energy Environ. Sci.* **2014**, *7* (10), 3192−3222.

(4) Martin, D. J.; Liu, G.; Moniz, S. J.; Bi, Y.; Beale, A. M.; Ye, J.; Tang, J. Efficient visible driven photocatalyst, silver phosphate: performance, understanding and perspective. *Chem. Soc. Rev.* **2015**, *44* (21), 7808−7828.

(5) Marschall, R. Semiconductor Composites: Strategies for Enhancing Charge Carrier Separation to Improve Photocatalytic Activity. *Adv. Funct. Mater.* **2014**, *24* (17), 2421−2440.

(6) Zhang, J.; Liu, X.; Neri, G.; Pinna, N. Nanostructured Materials for Room-Temperature Gas Sensors. *Adv. Mater.* **2016**, *28* (5), 795−831.

(7) Wang, H.; Rogach, A. L. Hierarchical SnO_2 Nanostructures: Recent Advances in Design, Synthesis, and Applications. *Chem. Mater.* **2014**, *26* (1), 123−133.

(8) Zheng, H.; Li, Y.; Liu, H.; Yin, X.; Li, Y. Construction of heterostructure materials toward functionality. *Chem. Soc. Rev.* **2011**, *40* (9), 4506−4524.

(9) Jeong, H. M.; Kim, J. H.; Jeong, S. Y.; Kwak, C. H.; Lee, J. H. CoO-SnO Hollow Heteronanostructures: Facile Control of Gas Selectivity by Compositional Tuning of Sensing Materials via Galvanic Replacement. *ACS Appl. Mater. Interfaces* **2016**, *8*, 7877−7883.

(10) Ju, D. X.; Xu, H.; Xu, Q.; Gong, H. B.; Qiu, Z. W.; Guo, J.; Zhang, J.; Cao, B. Q. High triethylamine-sensing properties of NiO/

DOI: 10.1021/acssuschemeng.8b02842
ACS Sustainable Chem. Eng. 2018, 6, 12375−12384

SnO_2 hollow sphere P−N heterojunction sensors. *Sens. Actuators, B* **2015**, *215*, 39−44.
(11) Xue, X.; Xing, L.; Chen, Y.; Shi, S.; Wang, Y.; Wang, T. Synthesis and H_2S Sensing Properties of CuO-SnO_2 Core/Shell PN-Junction Nanorods. *J. Phys. Chem. C* **2008**, *112*, 12157−12160.
(12) Qiao, X. Q.; Hu, F. C.; Tian, F. Y.; Hou, D. F.; Li, D. S. Equilibrium and kinetic studies on MB adsorption by ultrathin 2D MoS_2 nanosheets. *RSC Adv.* **2016**, *6*, 11631−11636.
(13) Tang, Y. J.; Wang, Y.; Wang, X. L.; Li, S. L.; Huang, W.; Dong, L. Z.; Liu, C. H.; Li, Y. F.; Lan, Y. Q. Molybdenum Disulfide/Nitrogen-Doped Reduced Graphene Oxide Nanocomposite with Enlarged Interlayer Spacing for Electrocatalytic Hydrogen Evolution. *Adv. Energy Mater.* **2016**, *6* (12), 1600116.
(14) Yang, Y.; Fei, H.; Ruan, G.; Xiang, C.; Tour, J. M. Edge-oriented MoS_2 nanoporous films as flexible electrodes for hydrogen evolution reactions and supercapacitor devices. *Adv. Mater.* **2014**, *26* (48), 8163−8168.
(15) Qiao, X. Q.; Hu, F. C.; Hou, D. F.; Li, D. S. PEG assisted hydrothermal synthesis of hierarchical MoS_2 microspheres with excellent adsorption behavior. *Mater. Lett.* **2016**, *169*, 241−245.
(16) Gu, X.; Cui, W.; Li, H.; Wu, Z.; Zeng, Z.; Lee, S. T.; Zhang, H.; Sun, B. A Solution-Processed Hole Extraction Layer Made from Ultrathin MoS_2 Nanosheets for Efficient Organic Solar Cells. *Adv. Energy Mater.* **2013**, *3* (10), 1262−1268.
(17) Liu, X.; Xing, Z.; Zhang, Y.; Li, Z.; Wu, X.; Tan, S.; Yu, X.; Zhu, Q.; Zhou, W. Fabrication of 3D flower-like black N-TiO_{2-x}@MoS_2 for unprecedented-high visible-light-driven photocatalytic performance. *Appl. Catal., B* **2017**, *201*, 119−127.
(18) Zhao, W.; Liu, Y.; Wei, Z.; Yang, S.; He, H.; Sun, C. Fabrication of a novel p−n heterojunction photocatalyst n-$BiVO_4$@p-MoS_2 with core−shell structure and its excellent visible-light photocatalytic reduction and oxidation activities. *Appl. Catal., B* **2016**, *185*, 242−252.
(19) Huang, Y.; Miao, Y. E.; Zhang, L.; Tjiu, W. W.; Pan, J.; Liu, T. Synthesis of few-layered MoS_2 nanosheet-coated electrospun SnO_2 nanotube heterostructures for enhanced hydrogen evolution reaction. *Nanoscale* **2014**, *6* (18), 10673−10679.
(20) Zhang, D.; Sun, Y.; Li, P.; Zhang, Y. Facile Fabrication of MoS_2-Modified SnO_2 Hybrid Nanocomposite for Ultrasensitive Humidity Sensing. *ACS Appl. Mater. Interfaces* **2016**, *8* (22), 14142−14149.
(21) Liu, C.; Kong, D.; Hsu, P. C.; Yuan, H.; Lee, H. W.; Liu, Y.; Wang, H.; Wang, S.; Yan, K.; Lin, D.; Maraccini, P. A.; Parker, K. M.; Boehm, A. B.; Cui, Y. Rapid water disinfection using vertically aligned MoS_2 nanofilms and visible light. *Nat. Nanotechnol.* **2016**, *11* (12), 1098−1104.
(22) Zhang, C. L.; Yu, S. H. Nanoparticles meet electrospinning: recent advances and future prospects. *Chem. Soc. Rev.* **2014**, *43* (13), 4423−4448.
(23) Zhang, H.; Zhu, Q.; Zhang, Y.; Wang, Y.; Zhao, L.; Yu, B. One-Pot Synthesis and Hierarchical Assembly of Hollow Cu_2O Microspheres with Nanocrystals-Composed Porous Multishell and Their Gas-Sensing Properties. *Adv. Funct. Mater.* **2007**, *17* (15), 2766−2771.
(24) Xie, J.; Zhang, J.; Li, S.; Grote, F.; Zhang, X.; Zhang, H.; Wang, R.; Lei, Y.; Pan, B.; Xie, Y. Controllable disorder engineering in oxygen-incorporated MoS_2 ultrathin nanosheets for efficient hydrogen evolution. *J. Am. Chem. Soc.* **2013**, *135* (47), 17881−17888.
(25) Chatti, M.; Gengenbach, T.; King, R.; Spiccia, L.; Simonov, A. N. Vertically Aligned Interlayer Expanded MoS_2 Nanosheets on a Carbon Support for Hydrogen Evolution Electrocatalysis. *Chem. Mater.* **2017**, *29* (7), 3092−3099.
(26) Kim, C.; Jung, J. W.; Yoon, K. R.; Youn, D. Y.; Park, S.; Kim, I. D. A High-Capacity and Long-Cycle-Life Lithium-Ion Battery Anode Architecture: Silver Nanoparticle-Decorated SnO_2/NiO Nanotubes. *ACS Nano* **2016**, *10*, 11317−11326.
(27) Hao, C.; Wen, F.; Xiang, J.; Wang, L.; Hou, H.; Su, Z.; Hu, W.; Liu, Z. Controlled Incorporation of $Ni(OH)_2$ Nanoplates Into Flowerlike MoS_2 Nanosheets for Flexible All-Solid-State Supercapacitors. *Adv. Funct. Mater.* **2014**, *24* (42), 6700−6707.
(28) Yang, D. J.; Kamienchick, I.; Youn, D. Y.; Rothschild, A.; Kim, I. D. Ultrasensitive and Highly Selective Gas Sensors Based on Electrospun SnO_2 Nanofibers Modified by Pd Loading. *Adv. Funct. Mater.* **2010**, *20* (24), 4258−4264.
(29) Zou, Y. H.; Chen, S.; Sun, J.; Liu, J. Q.; Che, Y. K.; Liu, X. H.; Zhang, J.; Yang, D. J. Highly Efficient Gas Sensor Using a Hollow SnO_2 Microfiber for Triethylamine Detection. *ACS Sens.* **2017**, *2*, 897−902.
(30) Chen, X.; Guo, Z.; Xu, W. H.; Yao, H. B.; Li, M. Q.; Liu, J.-H.; Huang, X.-J.; Yu, S. H. Templating Synthesis of SnO_2 Nanotubes Loaded with Ag_2O Nanoparticles and Their Enhanced Gas Sensing Properties. *Adv. Funct. Mater.* **2011**, *21* (11), 2049−2056.
(31) Wang, P. P.; Sun, H. Y.; Ji, Y. J.; Li, W. H.; Wang, X. Three-Dimensional Assembly of Single-Layered MoS_2. *Adv. Mater.* **2014**, *26*, 964−969.
(32) Cui, S. M.; Wen, Z. H.; Huang, X. K.; Chang, J. B.; Chen, J. H. Stabilizing MoS_2 Nanosheets through SnO_2 Nanocrystal Decoration for High-Performance Gas Sensing in Air. *Small* **2015**, *11* (19), 2305−2313.
(33) Ekspong, J.; Sharifi, T.; Shchukarev, A.; Klechikov, A.; Wågberg, T.; Gracia-Espino, E. Stabilizing Active Edge Sites in Semicrystalline Molybdenum Sulfide by Anchorage on Nitrogen-Doped Carbon Nanotubes for Hydrogen Evolution Reaction. *Adv. Funct. Mater.* **2016**, *26*, 6766−6776.
(34) Ju, D. X.; Xu, H. Y.; Qiu, Z. W.; Guo, J.; Zhang, J.; Cao, B. Q. Highly sensitive and selective triethylamine-sensing properties of nanosheets directly grown on ceramic tube by forming NiO/ZnO PN heterojunction. *Sens. Actuators, B* **2014**, *200*, 288−296.
(35) Li, W.; Xu, H.; Zhai, T.; Yu, H.; Chen, Z.; Qiu, Z.; Song, X.; Wang, J.; Cao, B. Enhanced triethylamine sensing properties by designing Au@SnO_2/MoS_2 nanostructure directly on alumina tubes. *Sens. Actuators, B* **2017**, *253*, 97−107.
(36) Sui, L. L.; Xu, Y. M.; Zhang, X. F.; Cheng, X. L.; Gao, S.; Zhao, H.; Cai, Z.; Huo, L. H. Construction of three-dimensional flower-like α-MoO_3 with hierarchical structure for highly selective triethylamine sensor. *Sens. Actuators, B* **2015**, *208*, 406−414.
(37) Wang, Y. L.; Jiang, X.; Xia, Y. N. A Solution-Phase, Precursor Route to Polycrystalline SnO_2 Nanowires That Can Be Used for Gas Sensing under Ambient Conditions. *J. Am. Chem. Soc.* **2003**, *125* (52), 16176−16177.
(38) Kolmakov, A.; Klenov, D. O.; Lilach, Y.; Stemmer, S.; Moskovits, M. Enhanced Gas Sensing by Individual SnO_2 Nanowires and Nanobelts Functionalized with Pd Catalyst Particles. *Nano Lett.* **2005**, *5*, 667−673.
(39) Xu, X. X.; Zhuang, J.; Wang, X. SnO_2 Quantum Dots and Quantum Wires: Controllable Synthesis, Self-Assembled 2D Architectures, and Gas-Sensing Properties. *J. Am. Chem. Soc.* **2008**, *130*, 12527−12535.
(40) Qiao, X. Q.; Zhang, Z. W.; Tian, F. Y.; Hou, D. F.; Tian, Z. F.; Li, D. S.; Zhang, Q. C. Enhanced catalytic reduction of p-nitrophenol on ultrathin MoS_2 nanosheets decorated noble-metal nanoparticles. *Cryst. Growth Des.* **2017**, *17* (6), 3538−3547.
(41) Wang, B.; Wang, Y.; Lei, Y.; Xie, S.; Wu, N.; Gou, Y.; Han, C.; Shi, Q.; Fang, D. Vertical SnO_2 nanosheet@SiC nanofibers with hierarchical architecture for high-performance gas sensors. *J. Mater. Chem. C* **2016**, *4* (2), 295−304.
(42) Motaung, D. E.; Mhlongo, G. H.; Makgwane, P. R.; Dhonge, B. P.; Cummings, F. R.; Swart, H. C.; Ray, S. S. Ultra-High Sensitive and Selective H_2 Gas Sensor Manifested by Interface of n−n Heterostructure of CeO_2 -SnO_2 Nanoparticles. *Sens. Actuators, B* **2018**, *254*, 984−995.
(43) Liu, C. B.; Wang, L. L.; Tang, Y. H.; Luo, S. L.; Liu, Y. T.; Zhang, S. Q.; Zeng, Y. X.; Xu, Y. Z. Vertical single or few-layer MoS_2 nanosheets rooting into TiO_2 nanofibers for highly efficient photocatalytic hydrogen evolution. *Appl. Catal., B* **2015**, *164*, 1−9.
(44) Xu, H. Y.; Ju, D. X.; Li, W. R.; Zhang, J.; Wang, J. Q.; Cao, B. Q. Superior triethylamine-sensing properties based on TiO_2/SnO_2 n-

DOI: 10.1021/acssuschemeng.8b02842
ACS Sustainable Chem. Eng. 2018, 6, 12375−12384

n heterojunction nanosheets directly grown on ceramic tubes. *Sens. Actuators, B* **2016**, *228*, 634−642.

(45) Ju, D.; Xu, H.; Xu, Q.; Gong, H.; Qiu, Z.; Guo, J.; Zhang, J.; Cao, B. High triethylamine-sensing properties of NiO/SnO_2 hollow sphere P−N heterojunction sensors. *Sens. Actuators, B* **2015**, *215*, 39−44.

(46) Hu, M.; Zhang, Z. W.; Luo, C. K.; Qiao, X. Q. One-Pot Green Synthesis of Ag-Decorated SnO_2 Microsphere: an Efficient and Reusable Catalyst for Reduction of 4-Nitrophenol. *Nanoscale Res. Lett.* **2017**, *12*, 435.

(47) Xu, G. W.; Wu, Y. P.; Dong, W. W.; Zhao, J.; Wu, X. Q.; Li, D. S.; Zhang, Q. C. A Multifunctional Tb-MOF for Highly Discriminative Sensing of Eu^{3+}/Dy^{3+} and as a Catalyst Support of Ag Nanoparticles. *Small* **2017**, *13*, 1602996.

DOI: 10.1021/acssuschemeng.8b02842
ACS Sustainable Chem. Eng. 2018, 6, 12375−12384